Nanomechanical systems in quantum information science

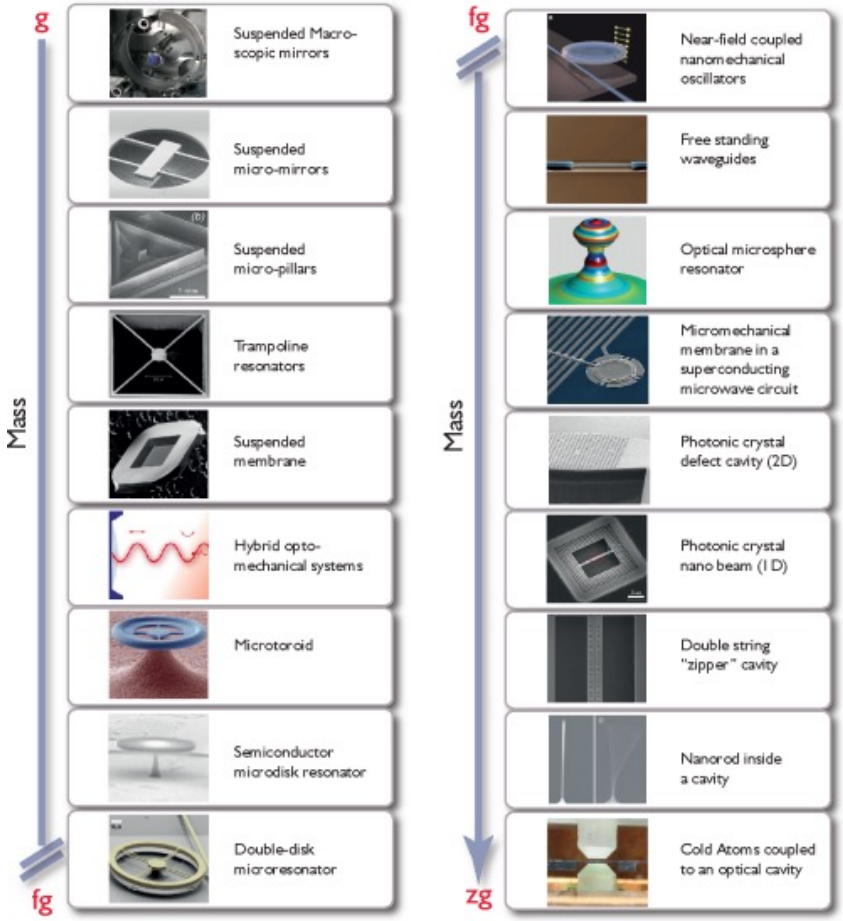

The generic cavity optomechanical system (input-output theory)

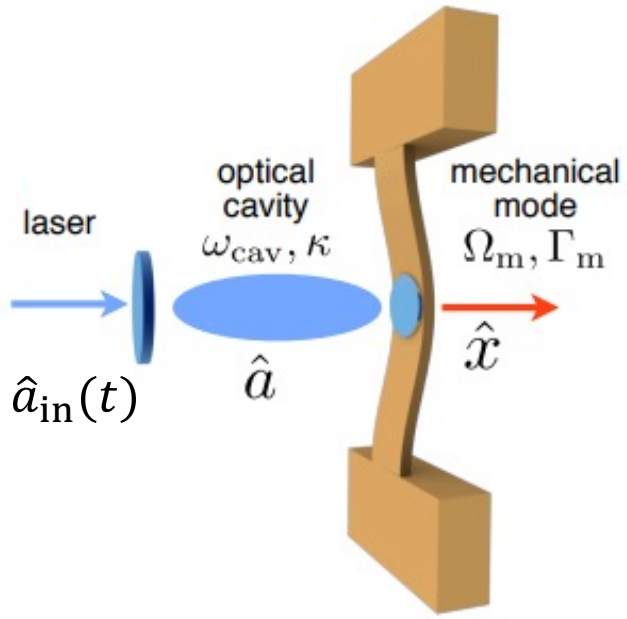

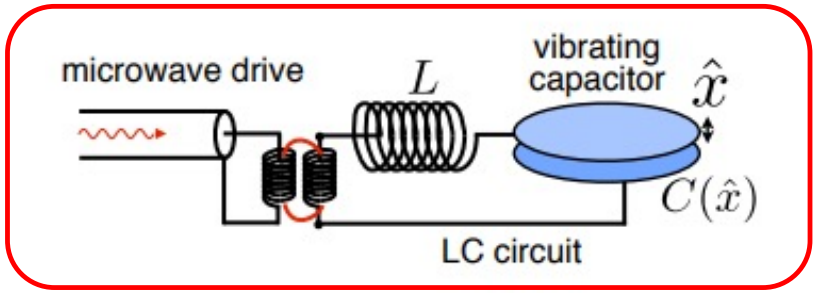

$$\dot{\hat{a}} = -\frac{\kappa}{2}\hat{a} + i\Delta\hat{a} + \sqrt{\kappa_{\mathrm{ex}}}\hat{a}_{\mathrm{in}} + \sqrt{\kappa_0}\hat{f}_{\mathrm{in}}$$

with a stochastic quantum input field $\hat{a}_{in}(t)$ normalized such that

$$P = \hbar\omega_{\mathrm{cav}}\langle\hat{a}_{\mathrm{in}}^{\dagger}\hat{a}_{\mathrm{in}}\rangle$$

and a total cavity loss rate given by

$$\kappa = \kappa_{\mathrm{ex}} + \kappa_0$$

According to the input-output theory of open quantum systems, the field coupled out of an OM system can be written

$$\hat{a}_{out} = \hat{a}_{in} - \sqrt{\kappa_{ex}}\hat{a}$$

Cavity Optomechanics, Aspelmeyer et. al., Rev. Mod. Phys. 86

Quantum motion of a nanomechanical resonator

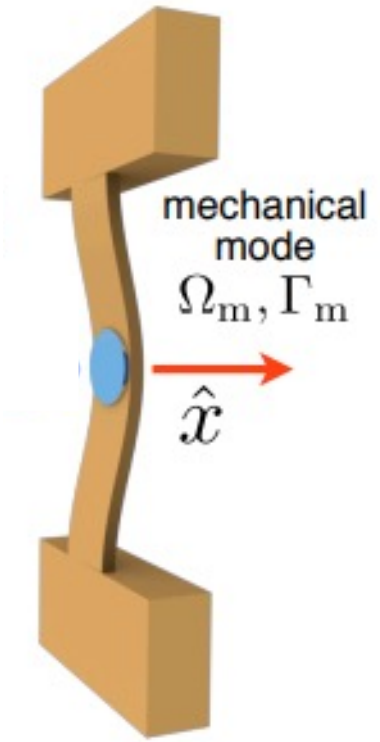

$$m_{eff}\frac{dx^2(t)}{dt^2} + m_{eff}\Gamma_m\frac{dx(t)}{dt} + m_{eff}\Omega_m^2 x(t) = F_{ext}(t)$$

$$\chi_{xx}(\omega) = \frac{1}{m_{eff}(\Omega_m^2 - \omega^2) - i m_{eff}\Gamma_m\omega}$$

$$\hat{H} = \hbar\Omega_m \hat{b}^\dagger \hat{b} + \frac{1}{2}\hbar\Omega_m\,, \quad \bar{n} = \langle \hat{b}^\dagger \hat{b} \rangle$$

Cavity Optomechanics, Aspelmeyer et. al., Rev. Mod. Phys. 86

Quantum motion of a nanomechanical resonator

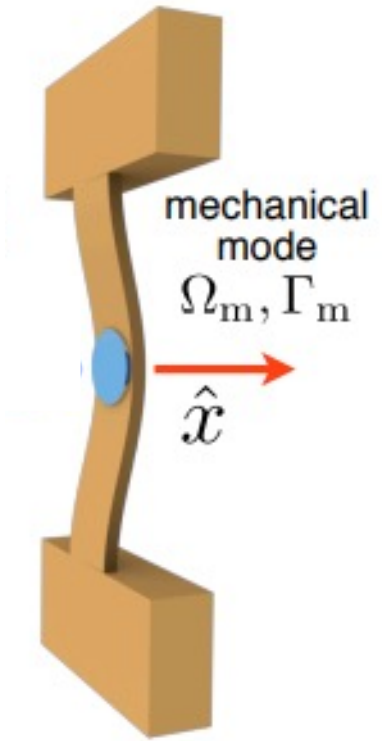

$$\hat{x} = x_{ZPF}\left(\hat{b} + \hat{b}^{\dagger}\right), \hat{p} = -im_{eff}\Omega_m x_{ZPF}\left(\hat{b} - \hat{b}^{\dagger}\right)$$

$$x_{ZPF}^2 = \langle 0|\hat{x}^2|0\rangle$$

$$x_{ZPF} = \sqrt{\frac{\hbar}{2m_{eff}\Omega_m}}$$

$$[\hat{x}_{ZPF}, \hat{p}_{ZPF}] = i\hbar$$

Cavity Optomechanics, Aspelmeyer et. al., Rev. Mod. Phys. 86

Mechanical dissipation and decoherence

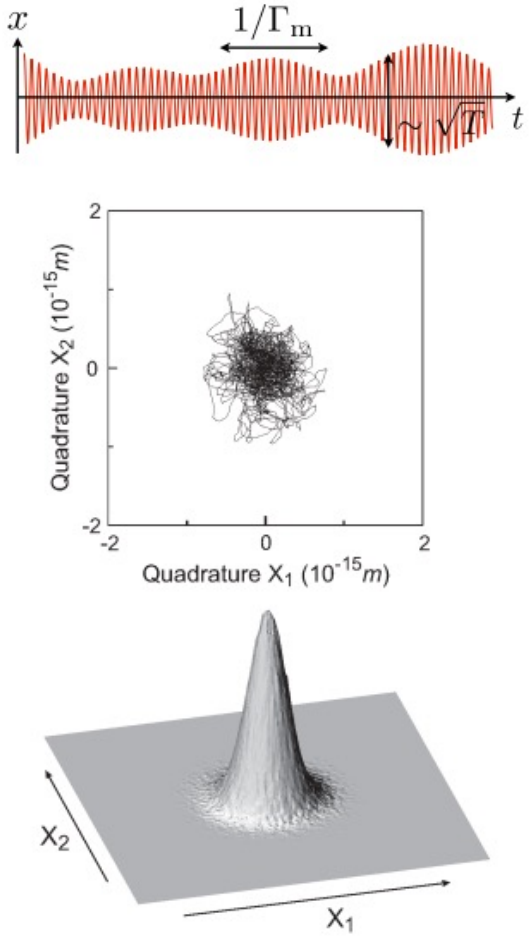

$$\Gamma_m = \frac{\Omega_m}{Q_m}$$

$$\frac{d}{dt}\langle n\rangle = -\Gamma_m(\langle n\rangle - \bar{n}_{th})$$

$$\frac{d}{dt}\langle n(t=0)\rangle = \bar{n}_{th}\cdot\Gamma_m \approx \frac{k_B T_{bath}}{\hbar Q_m}$$

Cavity Optomechanics, Aspelmeyer et. al., Rev. Mod. Phys. 86

Mechanical dissipation and decoherence

Some well-known loss mechanisms:

- Viscous damping (interaction with gas atoms)
- Clamping losses (elastic coupling to the oscillator's supports)
- Anharmonic effects (thermoelastic damping, phonon-phonon interactions
- Material loss (relaxation of intrinsic/extrinsic material defect states)

$$\frac{1}{Q_{total}} = \sum \frac{1}{Q_i}$$

Number of coherent oscillations in the presence of thermal decoherence:

$$\frac{\Omega_m}{\bar{n}_{th}\Gamma_m} = Q_m \cdot f_m \times \left(\frac{h}{k_B T}\right)$$

Cavity Optomechanics, Aspelmeyer et. al., Rev. Mod. Phys. 86

Optomechanical coupling

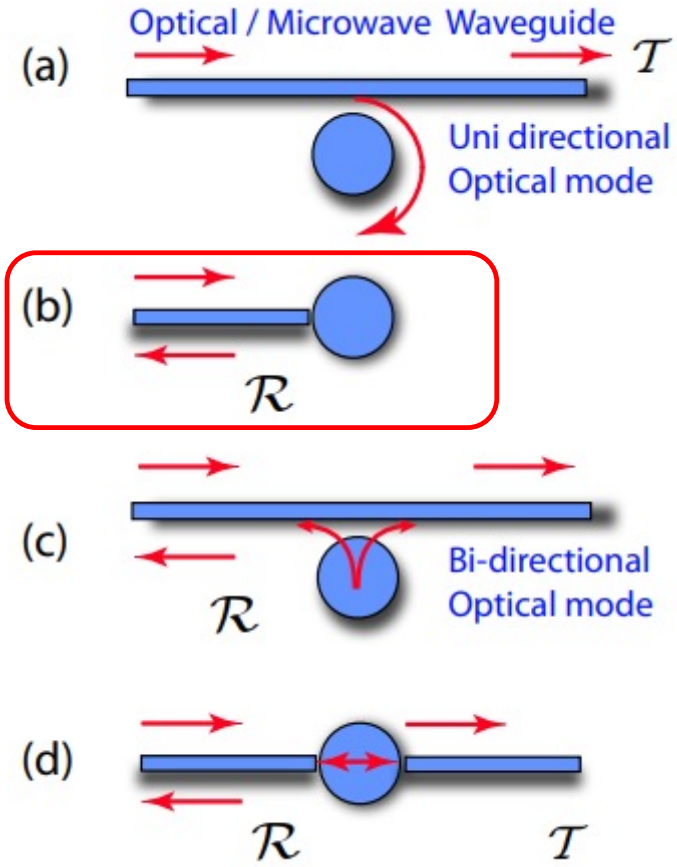

$$\mathcal{R} = \frac{\langle \hat{a}_{out} \rangle}{\langle \hat{a}_{in} \rangle} = \frac{(\kappa_0 - \kappa_{ex})/2 - i\Delta}{(\kappa_0 + \kappa_{ex})/2 - i\Delta}$$

$$|\Delta p| = 2h/\lambda$$

$$\langle \hat{F} \rangle = 2\hbar k \frac{\langle \hat{a}^\dagger \hat{a} \rangle}{\tau_c} = \hbar G \langle \hat{a}^\dagger \hat{a} \rangle , G = \frac{\omega}{L}$$

Cavity Optomechanics, Aspelmeyer et. al., Rev. Mod. Phys. 86

Optomechanical coupling

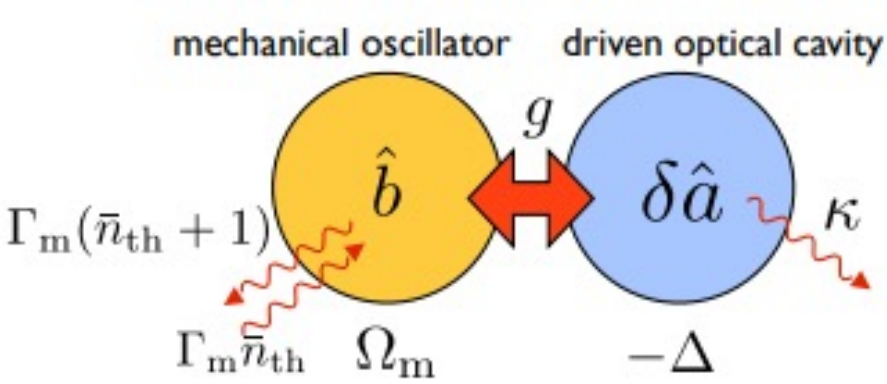

$$\hbar\omega_{cav}(x)\hat{a}^\dagger\hat{a} \approx \hbar(\omega_{cav} - G\hat{x})\hat{a}^\dagger\hat{a}$$

$$\hat{x} = x_{ZPF}\left(\hat{b} + \hat{b}^\dagger\right)$$

$$\hat{H}_0 = \hbar\Omega_m\hat{b}^\dagger\hat{b} + \hbar\omega_{cav}\hat{a}^\dagger\hat{a}$$

$$\hat{H}_{int} = -\hbar g_0\hat{a}^\dagger\hat{a}\left(\hat{b} + \hat{b}^\dagger\right)$$

$$g_0 = Gx_{ZPF}\ [\mathrm{Hz}]$$

Note: This interaction is fundamentally nonlinear - it contains three operators (three wave mixing)

Cavity Optomechanics, Aspelmeyer et. al., Rev. Mod. Phys. 86

Optomechanical coupling

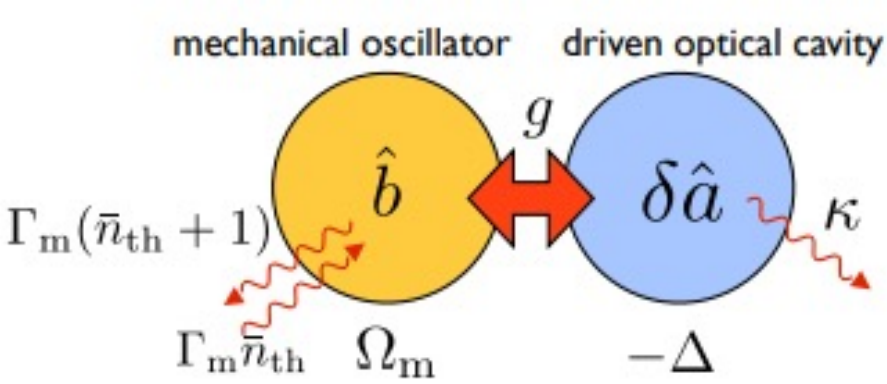

If we split the cavity field into a coherent amplitude $\langle\hat{a}\rangle = \bar{\alpha}$ and a fluctuating term,

$$\hat{a} = \bar{\alpha} + \delta\hat{a}\ ,$$

assume the coherent amplitude is real-valued

$$\bar{\alpha} = \sqrt{\bar{n}_{cav}}\ ,$$

and move to a frame rotating with the laser field ω_L, the Hamiltonian can be linearized and is given by

$$\widehat{H} \approx -\hbar\Delta\delta\hat{a}^{\dagger}\delta\hat{a} + \hbar\Omega_m\hat{b}^{\dagger}\hat{b} + \widehat{H}_{int}^{(\mathrm{lin})} + \cdots$$

Cavity Optomechanics, Aspelmeyer et. al., Rev. Mod. Phys. 86

Optomechanical coupling

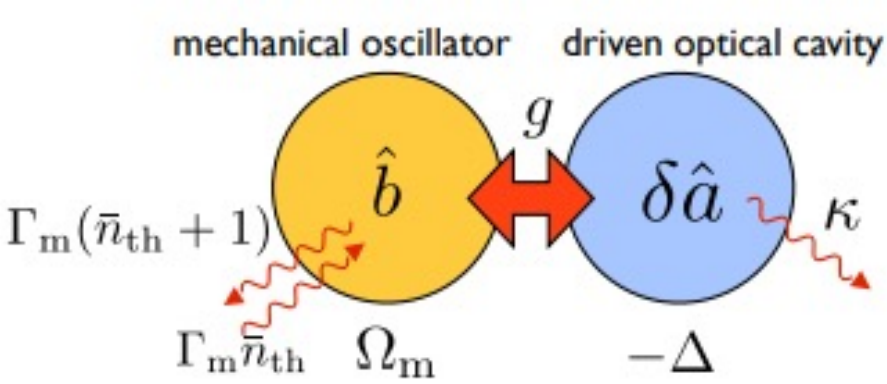

With an optomechanical coupling given by

$$g = g_0\sqrt{\bar{n}_{cav}}$$

The (now linearized) quadratic interaction part of $\hat{H}$ becomes can be expressed

$$\hat{H}_{int}^{(\mathrm{lin})} = -\hbar g\left(\delta\hat{a}^{\dagger} + \delta\hat{a}\right)\left(\hat{b} + \hat{b}^{\dagger}\right)$$

Cavity Optomechanics, Aspelmeyer et. al., Rev. Mod. Phys. 86

Optomechanical “beam splitter” interaction

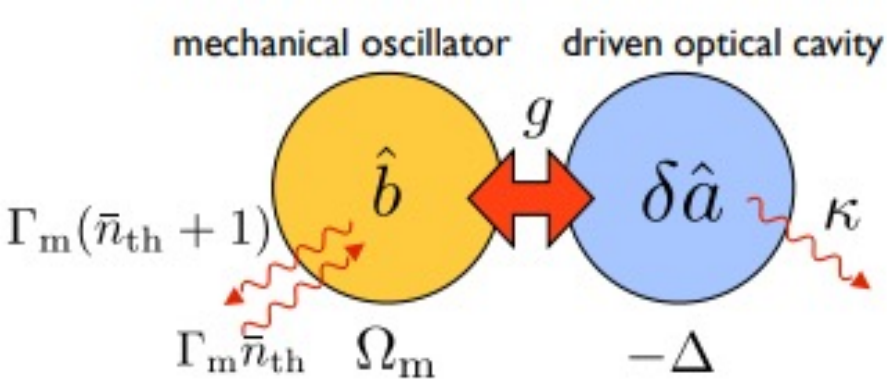

For a sideband-resolved ($\kappa \ll \Omega_m$) system within the rotating wave approximation and a detuning

$$\Delta = \omega_L - \omega_{cav} \approx -\Omega_m$$

we can write the “beam splitter” interaction between the two coupled harmonic oscillators as

$$-\hbar g\left(\delta\hat{a}^\dagger\hat{b} + \delta\hat{a}\hat{b}^\dagger\right)$$

Cavity Optomechanics, Aspelmeyer et. al., Rev. Mod. Phys. 86

Superconducting qubits in microwave circuits

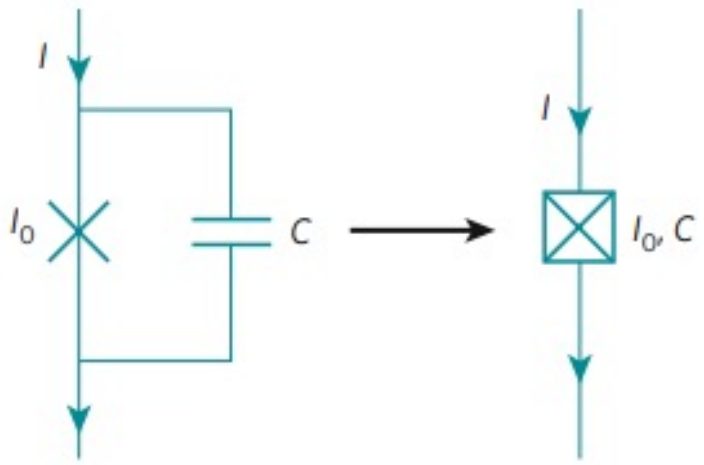

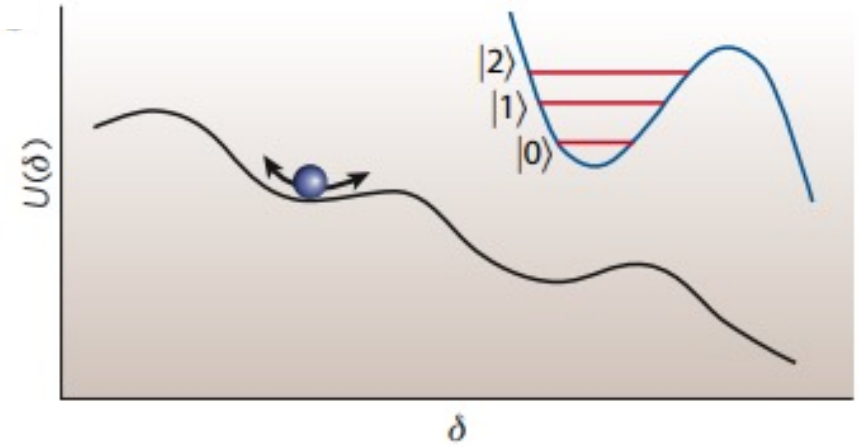

The Josephson Junction has a supercurrent that varies as the phase difference between its superconductors

$$I = I_0 \sin(\delta(t))$$

And a nonlinear inductance given by

$$\left|L_j\right| = \Phi_0/(2\pi I_0 \cos\delta) = \Phi_0/2\pi\sqrt{I_0^2 - I^2}$$

Which is responsible for the anharmonicity of its "washboard" potential well

Superconducting quantum bits, J. Clarke and F.K. Wilhelm, Nature 453

Superconducting qubits in microwave circuits

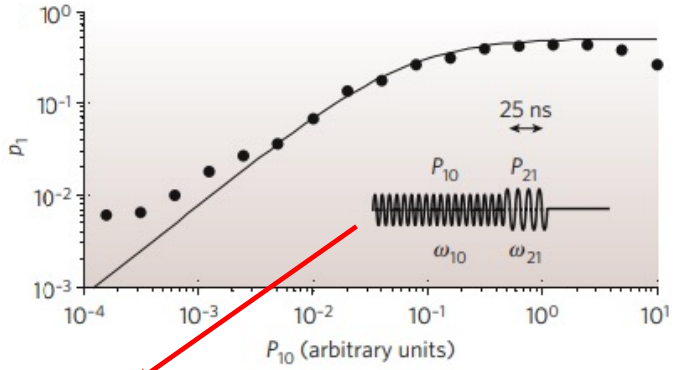

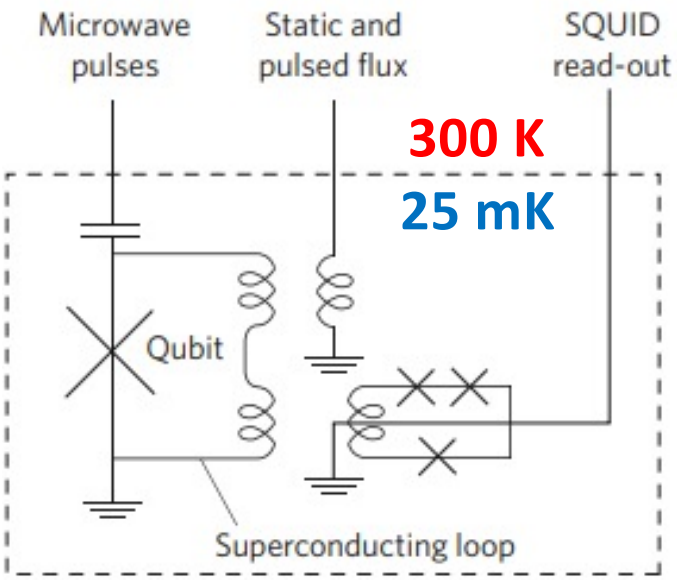

Despite configuration (flux, phase, etc.), superconducting qubits are operated in the microwave regime

Microwave photons containing quantum information are localized in mK circuits

What if SC qubits were optically addressable?

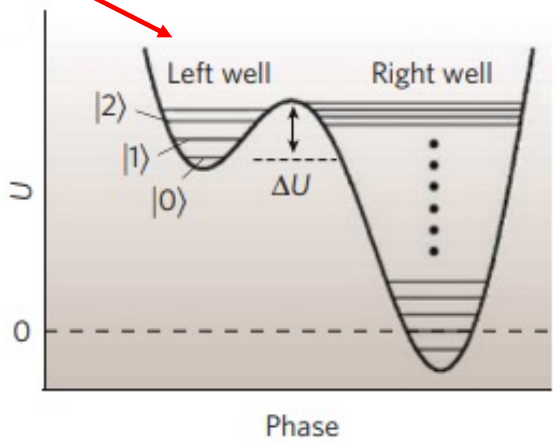

Superconducting quantum bits, J. Clarke and F.K. Wilhelm, Nature 453

Microwave-optical conversion

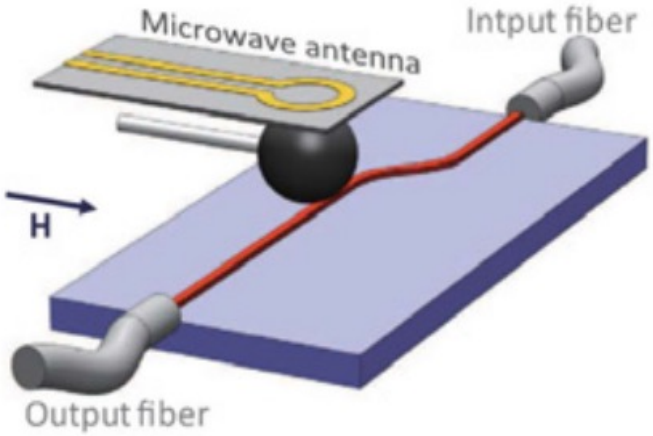

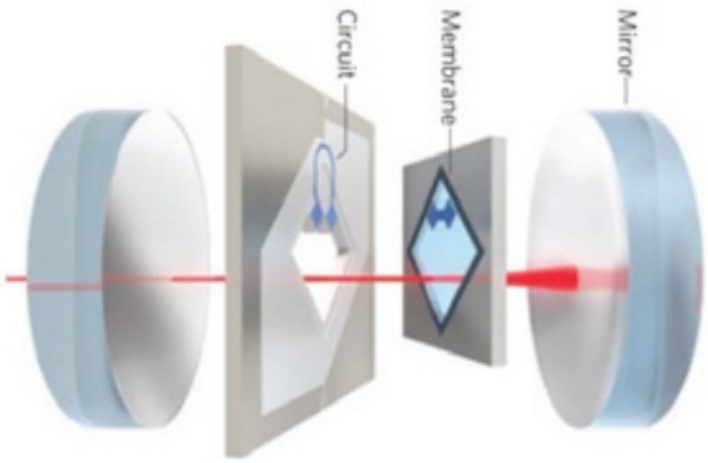

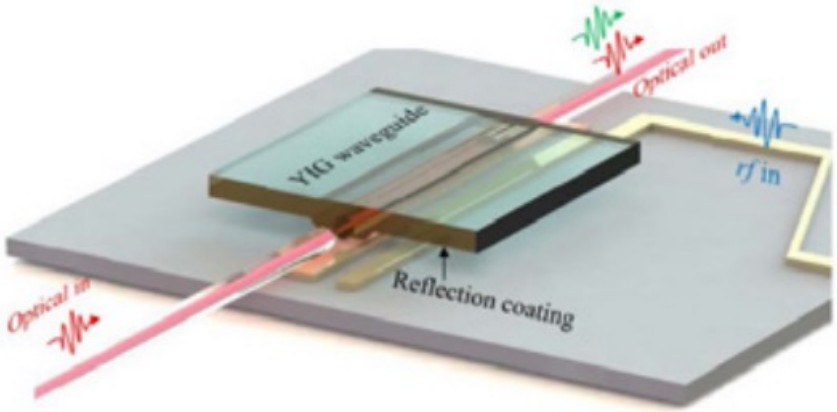

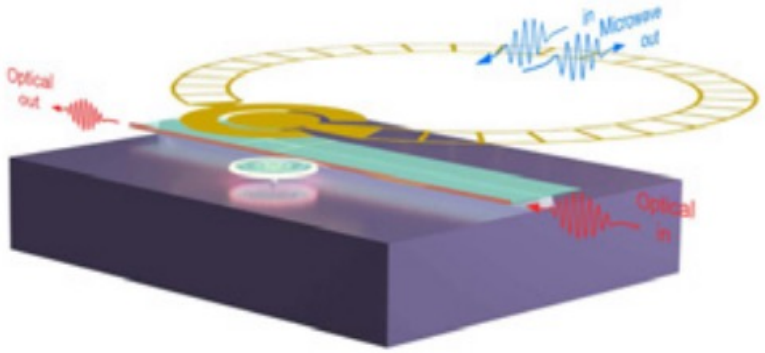

Microwave-optical quantum frequency conversion, X. Han et. al., Optica 8-8

Microwave-optical conversion

Nonlinear processes play a crucial role in M-O conversion, and can be classified by their order in the interaction $\hat{H}$, with

$$\hat{H} = \hat{H}_1 + \hat{H}_2 + \hat{H}_3 + \hat{H}_4 + \cdots$$

External Drive

$$\hat{H}_1 = \hbar \sum_j \left(c_j m_j^\dagger + \text{h. c.} \right)$$

$\chi^{(1)}$ process, quadratic in mode creation/annihilation operators, linear in Heisenberg equation – e.g. piezoelectric effect

$$\hat{H}_2 = \hbar \sum_{j,k} \left(c_{j,k} m_j^\dagger m_k + c'_{j,k} m_j^\dagger m_k^\dagger + \text{h. c.} \right)$$

$\chi^{(2)}$ processes, nonlinear in Heisenberg equation, but includes effects of interest for coherent M-O conversion

$$\hat{H}_3 = \hbar \sum_{j,k,l} \left(c_{j,k,l} m_j^\dagger m_k^\dagger m_l^\dagger + c'_{j,k.l} m_j^\dagger m_k^\dagger m_l + \text{h. c.} \right)$$

... ...

Linear processes, since $\frac{dO}{dt} = i\hbar[H, O]$; $\hat{H}_3, \hat{H}_4$, … commutators with O generate quadratic or higher order terms

Interaction can be linearized to employ the input-output formalism of cavity optomechanics and harness the nonlinear processes for coherent linear conversion

Microwave-optical quantum frequency conversion, X. Han et. al., Optica 8-8

Microwave-optical conversion

	$\chi^{(1)}$ process	$\chi^{(2)}$ process
Electro-optic (EO)	Energy Mismatch	Electro-optic Modulator $H_{eo} = \hbar g_{eo,0} a^\dagger a (b + b^\dagger)$
Electromechanical (EM)	Piezoelectric Effect $H_{pz} = \hbar g_{pz} (b + b^\dagger)(m + m^\dagger)$	Moving Capacitor $H_{em} = \hbar g_{em,0} b^\dagger b (m + m^\dagger)$
Optomechanical (OM)	Energy Mismatch	Radiation Pressure $H_{om} = \hbar g_{om,0} a^\dagger a (m + m^\dagger)$
Magneto-optical (MO)	Energy Mismatch	Faraday Effect $H_{mago} = \hbar g_{mago,0} a^\dagger a (m + m^\dagger)$

For example, a red-detuned optical pump in the sideband resolved limit ($\omega_e \gg \kappa_o$) reduces

$$H_{eo} = \hbar g_{eo,0} a^\dagger a \left(b + b^\dagger\right)$$

To a familiar “beam splitter” formulation

$$H_{eo} = \hbar g_{eo} \left(a^\dagger b + b^\dagger a\right)$$

Microwave-optical quantum frequency conversion, X. Han et. al., Optica 8-8

Microwave-optical conversion

	$\chi^{(1)}$ process	$\chi^{(2)}$ process
Electro-optic (EO)	Energy Mismatch	Electro-optic Modulator $H_{eo} = \hbar g_{eo,0} a^{\dagger} a (b + b^{\dagger})$
Electromechanical (EM)	Piezoelectric Effect $H_{pz} = \hbar g_{pz} (b + b^{\dagger})(m + m^{\dagger})$	Moving Capacitor $H_{em} = \hbar g_{em,0} b^{\dagger} b (m + m^{\dagger})$
Optomechanical (OM)	Energy Mismatch	Radiation Pressure $H_{om} = \hbar g_{om,0} a^{\dagger} a (m + m^{\dagger})$
Magneto-optical (MO)	Energy Mismatch	Faraday Effect $H_{mago} = \hbar g_{mago,0} a^{\dagger} a (m + m^{\dagger})$

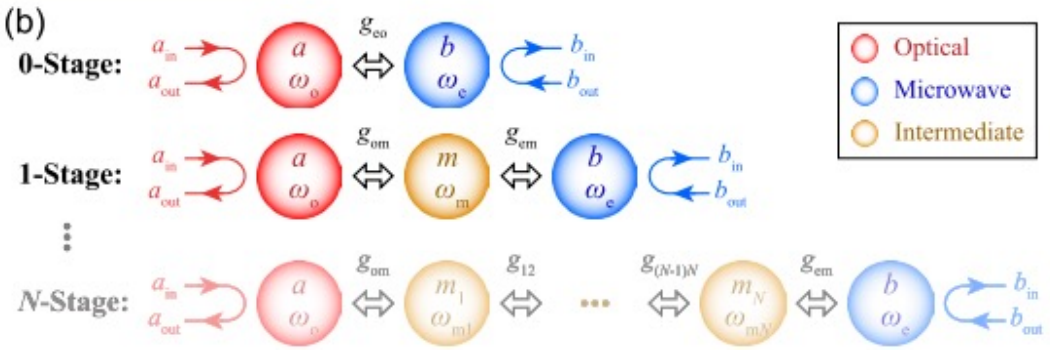

Microwave-optical quantum frequency conversion, X. Han et. al., Optica 8-8

Microwave-optical conversion with optomechanics platforms

MHz Electro-Optomechanics | GHz Piezo-Optomechanics

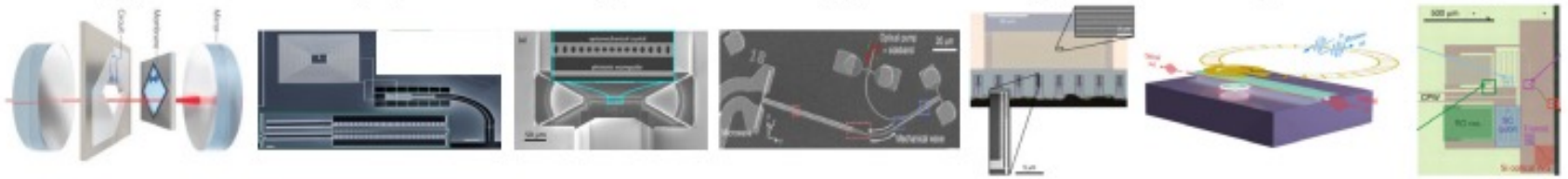

	(a)	(b)	(c)	(d)	(e)	(f)	(g)
$g_{om,0}$ [Hz]	6.6	0.66×10^6	115×10^3	80×10^3	1.3×10^6	19×10^3	$\sim 0.5 \times 10^6$
C_{om}	132	0.9	3×10^{-3}	5×10^{-3}	1.7	0.4	0.04
C_{em}	132	0.57	–	–	–	7	~ 150
η	0.47	1.9×10^{-4}	10^{-8}	10^{-5}	$< 3.5 \times 10^{-10}$	7.4×10^{-4}	8.8×10^{-6}
η_{in}	0.99	0.016	NR	0.026	NR	0.058	10^{-3}
$\frac{B}{2\pi}$ [MHz]	0.012	3.7×10^{-4}	~ 1	~ 1	NR	1	1
n_{add}	38	$\sim 10^4$	NR	NR	NR (*)	NR	0.57 (**)
T_{env} [K]	0.035	0.15	~ 300	~ 300	0.02	0.9	0.015

Microwave-optical quantum frequency conversion, X. Han et. al., Optica 8-8

Microwave-to-optics conversion using a mechanical oscillator in its ground state

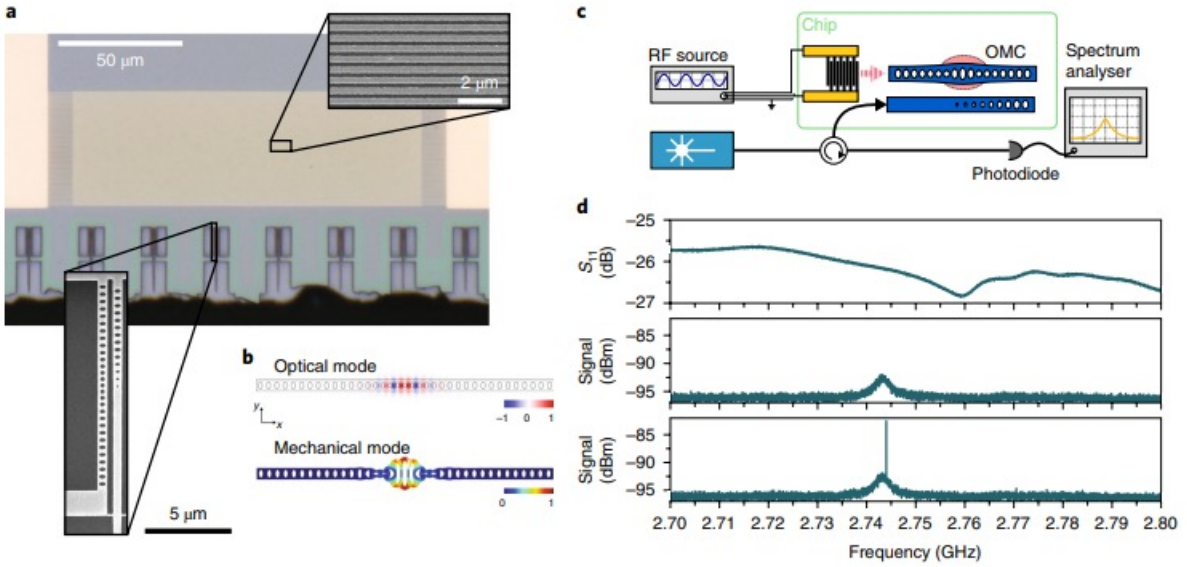

Fig. 1 | Device layout and room-temperature characterization. a, A micrograph of the transducer devices. Our structures are comprised of an IDT (in gold, see upper inset), which spans several optomechanical devices for ease of fabrication. The bottom side of the chip is directly accessible with a lensed fibre, allowing for optical access to the devices. The lower inset shows a scanning electron micrograph of an optomechanical resonator. The waveguide (right) is used for evanescently coupling light in and out of the device using the lensed fibre (accessed from the bottom, not shown). **b**, Finite-element simulations of the optomechanical device. The E_y component of the fundamental optical mode is shown (top) alongside the displacement field of the co-localized mechanical mode oscillating around 2.7 GHz (bottom). **c**, A schematic of the room-temperature characterization set-up. A laser is used to address the device optically. The reflected light is then measured on a high-speed photodiode to resolve the noise spectrum around the mechanical frequency while an RF source is used to drive the IDT. **d**, Upper panel: S_{11} reflection measurement of the IDT device with a resonance at 2.76 GHz. Lower panels: optical measurements of the gigahertz-frequency noise of the reflected light with (bottom) and without (centre) the RF drive tone applied to the IDT, which results in a narrow, coherent peak in the spectrum on top of the thermal peak. The laser in these measurements is blue-detuned from cavity resonance by the mechanical frequency, ω_m.

M. Forsch et. al., *Nature Physics* 16 (2020)

Microwave-to-optics conversion using a mechanical oscillator in its ground state

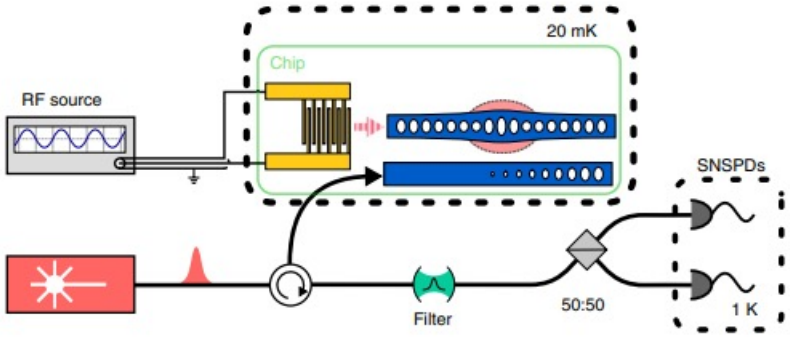

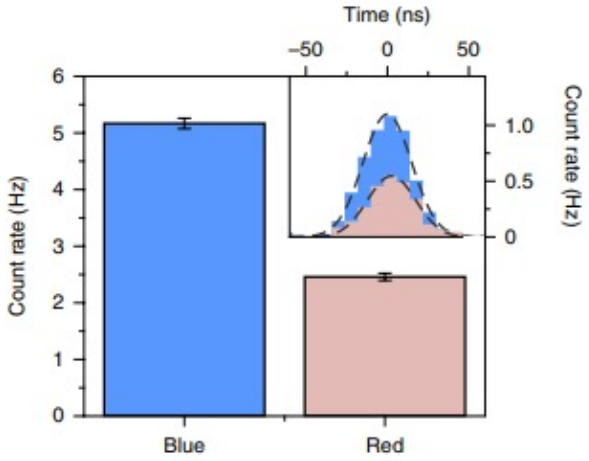

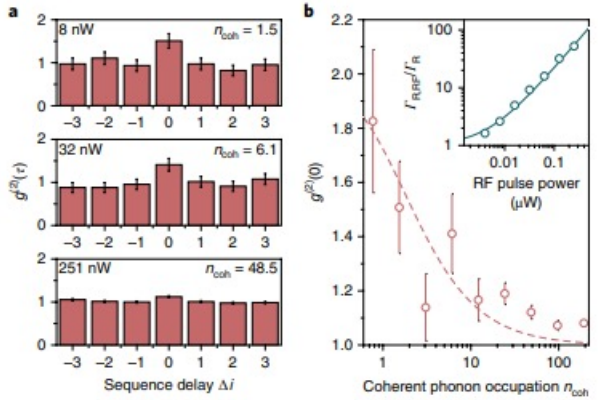

Fig. 3 | Correlation measurements of the microwave-to-optical transducer in the pulsed regime. a, The transducer is operated such that RF drive pulses are upconverted to the optical domain using optical readout pulses. Shown are the correlations between coinciding detection events on the two single-photon detectors for photons emerging from the same ($\Delta i = 0$) or different ($\Delta i \neq 0$) pulse sequences. The panels correspond to various coherent phonon populations. **b**, The full set of $g^{(2)}(0)$ values is shown as a function of RF power applied to the IDT. The dashed curve displays the expected value of $g^{(2)}(0)$ for a displaced thermal state with the corresponding extracted coherent phonon number n_{coh} (see Supplementary Information). The inset shows the relative increase in the count rate as a function of RF power with a linear fit. We use this to extract the ratio of n_{coh}/n_{th} which allows us to demonstrate the conversion at the single-coherent-phonon level for the lowest powers. We can see a clear transition from a bunched (low RF power) towards a not-bunched (high RF power) second-order correlation. All error bars are one standard deviation.

M. Forsch et. al., *Nature Physics* 16 (2020)

Resolving the energy levels of a nanomechanical oscillator

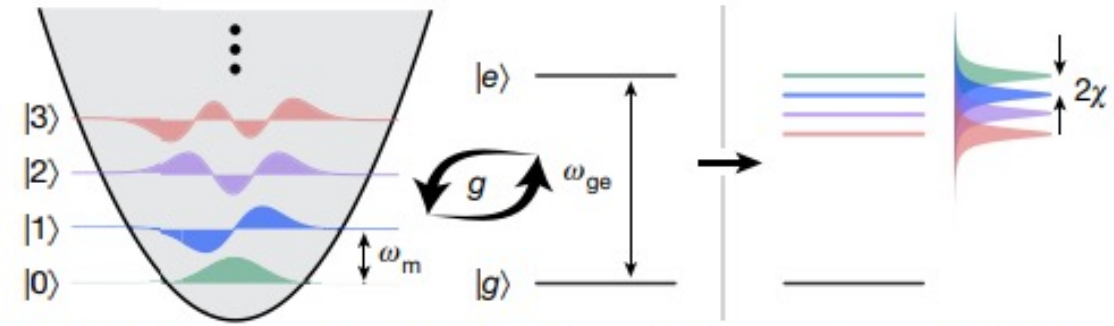

Fig. 1 | Phonon-number-splitting scheme. The state of a mechanical oscillator is described in quantum mechanics by a linear superposition of equally spaced energy eigenstates $|n\rangle$, each representing a state of n phonons in the system. This quantized structure is normally not resolvable because all of the transitions between the energy levels occur at the same frequency ω_m. By coupling the resonator to a qubit of transition frequency ω_{ge} with a rate of g, we cause splitting in the qubit spectrum that is parameterized by the dispersive coupling rate χ. This allows us to distinguish between the different phonon-number states that are present in the oscillator.

P. Arrangoiz-Arriola et. al., *Nature* 571

Resolving the energy levels of a nanomechanical oscillator

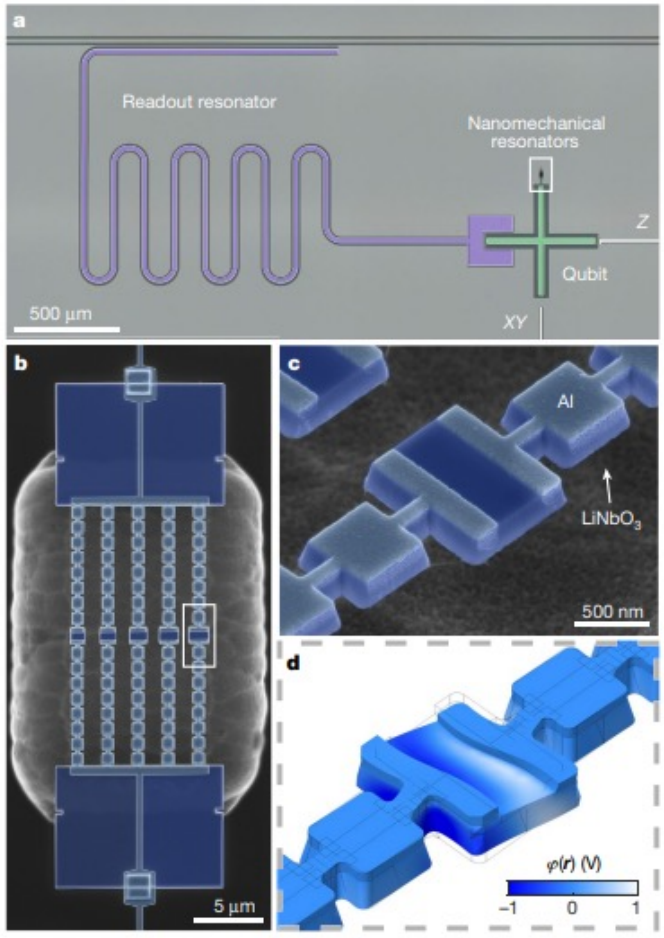

Fig. 2 | Fabricated device. a, False-colour optical micrograph of the device, showing the readout resonator (purple), transmon qubit (green) and nanomechanical resonators (white box). The qubit flux control (Z) and excitation (XY) lines are shown in white. **b**, False-colour scanning electron micrograph of the suspended resonators. Each resonator consists of a defect site embedded in a phononic crystal that supports a complete phononic bandgap in the frequency range ~2−2.4 GHz. The structures are fabricated from a 250-nm-thick film of lithium niobate (dark blue) that is suspended above a silicon substrate, and are coupled to the qubit via thin aluminium electrodes (light blue) that address the defect modes. We form a connection between the electrodes and the qubit using superconducting bandages, which are visible as small squares at the edges of the LN-supporting slabs. **c**, Scanning electron micrograph of a phononic crystal defect. **d**, Finite-element method simulation of a mechanical defect mode, showing the localized deformation of the structure and the electrostatic potential $\phi(\boldsymbol{r})$ (colour scale) generated through the piezoelectricity of LN.

P. Arrangoiz-Arriola et. al., *Nature* 571

Resolving the energy levels of a nanomechanical oscillator

Fig. 4 | Phonon-number splitting. The qubit excitation spectrum is measured following a phonon excitation pulse of duration $\tau_{mech} = 175$ ns and of varying amplitude (see inset for the pulse sequence). The detuning on the horizontal axis is relative to the qubit frequency $\omega_{ge}/2\pi = 2.317$ GHz in the absence of a phonon excitation pulse. The initial phonon populations prepared by the pulse decay over the course of the measurement but are nevertheless visible as individual peaks separated by twice the dispersive coupling rate, 2χ. At the highest drive amplitudes we are able to resolve states with phonon numbers up to $n = 3$. We fit the data (blue points) using numerical master-equation simulations of the full pulse sequence (solid grey lines), with the mechanical drive strength as the only free fit parameter in the Hamiltonian. From these simulations we extract the mean phonon number $\overline{n} = \langle \hat{n}(\tau_{mech} + \tau/2) \rangle$ midway through the qubit spectroscopy pulse, which we indicate next to each spectrum.

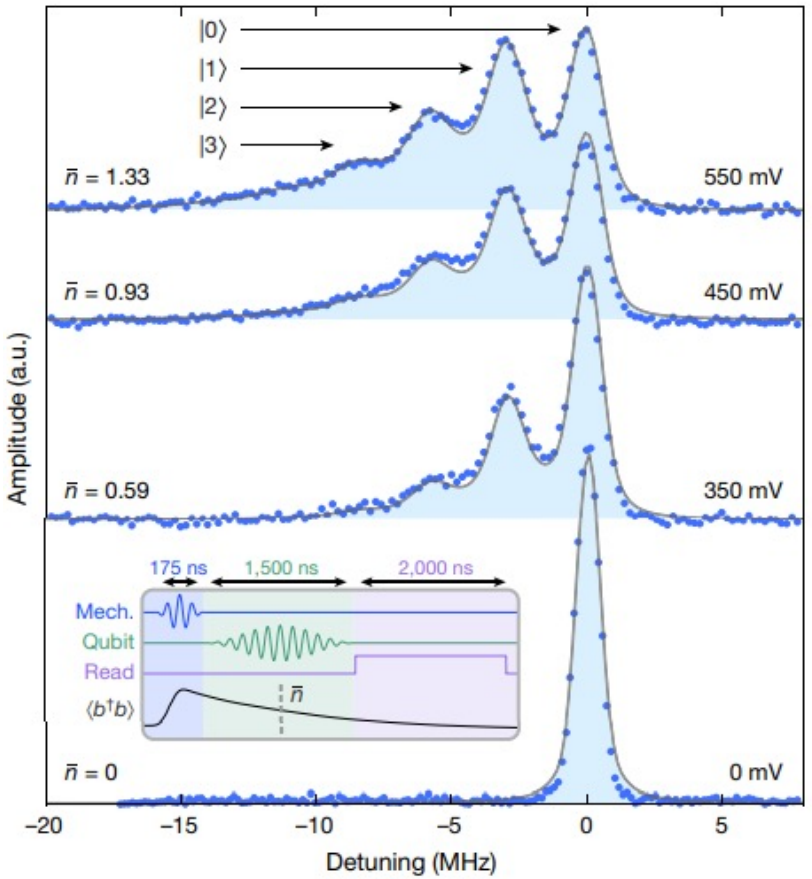

P. Arrangoiz-Arriola et. al., *Nature* 571

Superconducting circuit quantum computing with nanomechanical resonators as storage

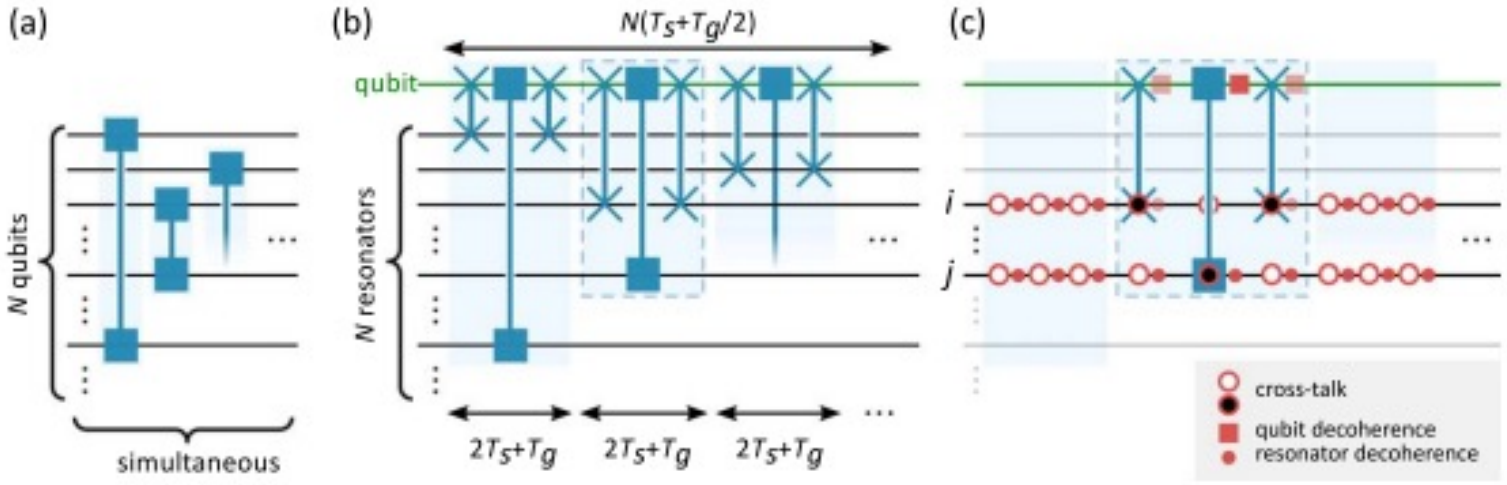

Figure 1. (a) Schematic representation of one step of a quantum circuit acting on N qubits. All two-qubit gates between distinct pairs of qubits are performed simultaneously. (b) Sequential version of the circuit from (a), with the single qubit mediating interactions between N resonators. Each effective two-resonator gate consists of two-qubit-resonator swap gates surrounding one arbitrary qubit-resonator gate. (c) The errors acting on a specific pair of resonators i and j in the sequential protocol. Decoherence errors are shown by solid circles (for the resonators) and squares (for the qubit). Cross-talk errors which occur because the gates acting on i and j also weakly address other resonators are shown by filled red circles. The other class of cross-talk errors, caused by gates performed on other resonators affecting i and j, is indicated by empty red circles.

M. Pechal et. al., *Quantum Sci. Technol. 4 015006*

Superconducting circuit quantum computing with nanomechanical resonators as storage

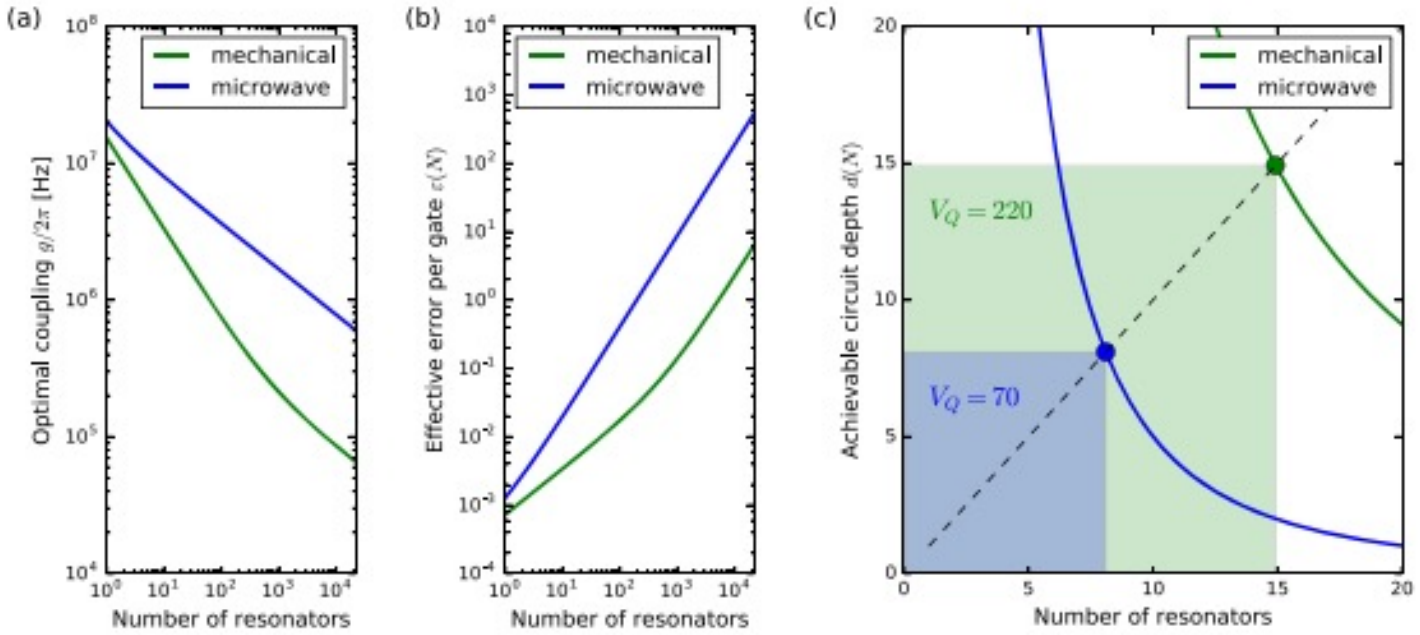

Figure 2. (a) Dependence of the optimal coupling which minimizes the effective gate error on the number of resonators N. (b) The effective error probability per gate achieved at the optimal coupling from (a) as a function of N. (c) Illustration of the quantum volume in the electromechanical and purely microwave implementation in a plot of the achievable circuit depth $d(N)$ as a function of N. Since $d(N)$ decreases with increasing N, the quantity $\min(N, d(N))$ is maximized when $N = d(N)$, as shown by the points indicating the intersection of the curves with the dashed diagonal line. The quantum volume is then the area of the filled squares.

M. Pechal et. al., *Quantum Sci. Technol. 4 015006*

Proposal for a nanomechanical qubit

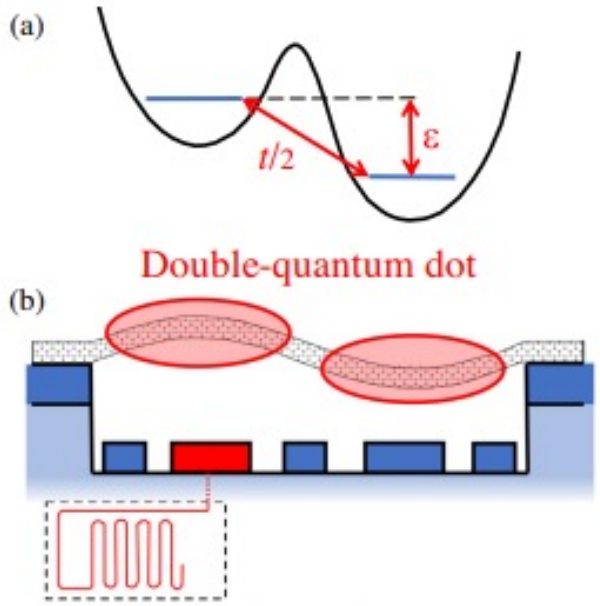

FIG. 1. Schematic of the proposed setup. A suspended carbon nanotube hosting a double quantum dot, whose one-electron charged state is coupled to the second flexural mode. (a) Sketch of the electronic confinement potential and of the two main parameters, the hopping amplitude t and the energy difference ϵ between the two single-charge states. (b) Physical realization. One of the gate electrodes is connected to a microwave cavity for dispersive qubit readout.

F. Pistolesi et. al., *Phys. Rev. X* 11, 031027 (2021)